Nanoscale

PAPER

View Article Online
View Journal | View Issue

Cite this: *Nanoscale*, 2024, **16**, 17176

Energy deposition in liquid scintillators composed of $CsPbBr_3$ colloidal nanocrystal dispersions†

M. Baravaglio, [a,c] B. Sabot, [b] F. Maddalena, [c] M. D. Birowosuto, [d] C. Dang, [c,f] C. Dujardin *[a,e] and B. Mahler *[a]

Received 11th June 2024,
Accepted 11th August 2024

DOI: 10.1039/d4nr02401j

rsc.li/nanoscale

Liquid scintillation processes are commonly used for various applications involving radioactivity levels analysis, as well as experiments in the field of high energy physics, most commonly in the form of organic scintillating cocktails. In this paper, we explore the potential of halide perovskite nanocrystal colloidal dispersions as an alternative to those organic mixtures. After an optimization of the nanocrystals' mean size and surface chemistry, the scintillation yield of these composite mixtures is evaluated through Compton – Triple to Double Coincidence Ratio experiments and compared with commercial liquid scintillator. The obtained results shine a light on the energy deposition mechanisms in nanocrystals-based liquid scintillators.

Introduction

Halide perovskite nanocrystals (PNCs) stand out in the nanomaterials field as semiconductors of ionic nature which were the first in the colloidal nanocrystals family to exhibit bright photoluminescence (PL) over the entire visible spectral range without electronic surface passivation.[1] This exceptional PL, influenced by quantum-sized effects on excitonic emission, is accompanied by a high tolerance of the electronic properties to the material's defects and surfaces.[2]

The outstanding optical and electronic properties of these nanostructures made them emerge as one of the most promising materials in physics, chemistry and device engineering. This led to an exponential increase in the related published articles during the last two decades, with a vast variety of applications from photovoltaics to photocatalysis and optoelectronics, including light-emitting diodes (LEDs), colour conversion systems and quantum photonic technologies.[3–7]

These metal-halide perovskites can now be easily synthesized as colloidal nanocrystals that show narrow and bright luminescence (photoluminescence quantum yield PLQYs >90%) with short (ns to sub-ns) radiative lifetimes, tuneable emission wavelength, and through shape-controlled syntheses which are mostly easy and inexpensive.[8,9]

These exciting features, combined with the presence of heavy metals in the chemical composition, made them become a trending material in the scintillation field, where they make good candidates for realizing ionizing radiation detectors.[10–14] This field has a high interest since ionizing radiation detection has a crucial role in high-energy physics experiments, oil drilling explorations, diagnostic imaging, nuclear energy radiation protection, and homeland security.[15–18] Many examples of perovskite-based ionizing radiation detectors have been studied over the last 25 years:[19] a first branch involves perovskite bulk structures, more dense but less luminescent than the corresponding nanoparticles. A second branch focuses on perovskite colloidal nanocrystals embedded in plastic or resin matrices, which preserve the advantages of the bright and fast-emitting nanoparticles and give them good protection against humidity and oxygen, but inevitably decrease the overall composite density.[12,14,20–27] The overall density, nevertheless, is a key parameter for a good scintillator, since it impacts the stopping power of the material towards the ionizing radiation and thus the probability of interaction and the effective scintillation yield; other important parameters are high effective atomic number (Z_{eff}) (linked to the overall material density), high light yield, and short decay time for most of the applications and in particular all applications using coincidence time window or time of flight. Inexpensive and easy fabrication is also an important parameter when commercial application is foreseen. While an

[a]*Université Claude Bernard Lyon 1, Institut Lumière Matière UMR 5306, CNRS F-69622 Villeurbanne, France. E-mail: benoit.mahler@univ-lyon1.fr, christophe.dujardin@univ-lyon1.fr*
[b]*Université Paris Saclay, CEA, LIST, Laboratoire National Henri Becquerel (LNE-LNHB), F-91120 Palaiseau, France*
[c]*IRL 3288 CINTRA, CNRS-NTU-Thales, Nanyang Technological University, Research Techno Plaza, 50 Nanyang Drive, Singapore, 637553, Singapore*
[d]*Łukasiewicz Research Network—PORT Polish Center for Technology Development, Stabłowicka 147, 54-066 Wrocław, Poland*
[e]*Institut Universitaire de France (IUF), France*
[f]*School of Electrical and Electronic Engineering, Nanyang Technological University, Singapore, 639798, Singapore*

†Electronic supplementary information (ESI) available: Additional characterizations, treatments with different ligands. See DOI: https://doi.org/10.1039/d4nr02401j

ideal scintillator that excels in each of these properties has yet to be found, commercial solid-state scintillators and liquid scintillators have limitations that hinder their broad application. Solid-state scintillators tend to be expensive and exhibit "incomplete" scintillation properties, whereas commercial liquid scintillators suffer from their relatively low effective atomic number and modest light yield, which hinder their further usage.

Nevertheless, these liquid mixtures show excellent damage resistance, fast decay time, low cost and exceptional scalability. Consequently, they find numerous applications for daily life analytical tests, such as radioactivity level measurements for environmental, medical and security purposes, and in the study of biochemical reaction mechanisms by radionuclide labelling. They are also used in huge international experiments for β-emissions and neutrino detection, such as KamLAND, Daya Bay, and RENO.[28–34] However, as previously stated, the organic composition of these systems makes them a low density, and thus an unsatisfying stopping power for other applications.

In this context, halide perovskite nanocrystals have recently started to raise interest in the liquid scintillation field, owing to their bright, tuneable emissions, their fast decay time and high effective atomic number. Nevertheless, to our knowledge, their assessment thus far has primarily been confined to their role as wavelength shifters while the energy transfer was from excited solvents to organic dyes.[35–38]

Consequently, the aim of this study has been to investigate the potential of colloidal dispersions of PNCs alone as liquid scintillators. This investigation focuses on the excitation mechanism of such nanoparticles in an organic solvent medium, with a specific emphasis on the possible energy transfers occurring between the organic solvent and the nanocrystals as they occur with dyes in commercial liquid scintillator mixtures. An efficient light-emission process and a high PNCs loading ratio hold the promise of mitigating the drawback of the low-density problem of the traditionally used organic liquid scintillators. This approach has also the potential to reduce the time-consuming amount of steps needed for the scintillation process. The liquid scintillation process was especially studied using the Triple to Double Coincidence Ratio (TDCR), which is based on a coincidence method and can give information about the light emission, self-absorption phenomena and the scintillation quantum yield,[39,40] a parameter which is not straightforward to evaluate in the case of nanostructures due to the complex energy deposition scheme under ionizing radiation excitation.[41]

In this paper, we studied the scintillation processes at play in colloidal dispersions of $CsPbBr_3$ nanocrystals. We first focused on enhancing the system performances, exploring different nanoparticle sizes, concentrations and surface chemical stabilization. The best PNC liquid scintillators were then used for Compton-TDCR experiments, allowing to shine a light on the energy deposition processes in binary PNCs/solvent mixtures.

Experimental

Chemicals

The following reagents were purchased and used as received. Anhydrous acetone (99.8%) and hexylamine (99%) were purchased from Acros, 2-aminoanthracene (96%), benzoic acid (≥99.5%), bromine (≥99.5%), caesium carbonate (99.9%), cynnamic acid (≥99.0%), 2,5-diphenyloxazole (99%), hydrobromic acid (48%, aqueous solution), lead acetate trihydrate (99.99%), phenethylammonium bromide (>98%), anhydrous toluene (99.8%) and trioctylphosphine (>97%) were purchased from Sigma Aldrich/Merck; 1-octadecene (90%), oleic acid (90%) were from Alfa-Aesar; diisopropylnaphthalene (>99.0%, isomer mixture) from Fisher.

Synthesis

Precursors. Cs-oleate was obtained by mixing caesium carbonate (6.4 mmol) and oleic acid (OA, 20.5 mmol) in octadecene (ODE, 21 mL) in a 50 mL three-neck flask, under vacuum at 65 °C, until completion of gas evolution. The resulting product was stored under an argon atmosphere. Similarly, Pb-oleate was obtained by mixing lead acetate (19 mmol) and oleic acid (38 mmol) in ODE (26 mL) in a 50 mL three-neck flask, under vacuum at 65 °C, until completion of gas evolution. The resulting product was stored under argon. TOP-Br_2 was synthesized in the glovebox in a 50 mL three-neck flask, by gently mixing trioctylphosphine TOP (18 mmol) with Br_2 (16 mmol) at room temperature: once the white crude cooled down at room temperature, it was dissolved in 26 mL of anhydrous toluene. All synthesized precursors are stored in an argon-filled glovebox.

Bromide salts of hexylamine and 2-aminoanthracene were obtained by mixing in a 50 mL three-neck flask 1.25 mmol of the starting amine and 0.280 mL of HBr aqueous solution in 20 mL of ethanol. The reaction mixture was left stirring under an argon atmosphere and in an icy water bath for 10 h. Once the reaction was over, the resulting solution was dried under vacuum, rinsed six times with diethylether and finally dried under vacuum at 80 °C. The final product was stored in the glovebox for further use.

Perovskite nanocrystals. The $CsPbBr_3$ nanocrystals were synthesized by scaling-up the procedure described by Krieg *et al.*:[42] in a 250 mL three-neck flask, Cs-oleate (8 mmol), Pb-oleate (12.5 mmol) and soy lecithin (2.5 mmol) were dissolved in 100 mL of ODE and degassed under vacuum at 50 °C for 1 h. The flask was then filled with Argon and the temperature was raised to 120 °C, and 25 mmol of TOP-Br_2 were injected swiftly; the flask was immediately quenched with icy water. The purification process involved three consecutive centrifugations at 9000 RCF for 2 minutes, adding acetone (twice the crude's volume) during the first two centrifuge steps and redispersing the precipitate in decreasing amounts of anhydrous toluene. The colloidal dispersion concentrations were evaluated by using the intrinsic absorption coefficient of $CsPbBr_3$ nanocrystals described by De Roo *et al.*[43]

Size selection. The different fractions were isolated *via* selective precipitation. First, 10 mL of the pristine sample, added with 10 mL of anhydrous acetone, were centrifuged at 10 000 RCF for 10 min: the supernatant, containing the smallest fraction of PNCs, was then added with 15 mL of anhydrous acetone and centrifuged again at 10 000 RCF overnight, and the resulting precipitate was finally redispersed in 10 mL of toluene (sample "S"). The precipitate from the first centrifugation, containing bigger PNCs, was then redispersed in 10 mL of toluene and centrifuged at 10 000 RCF for 30 min: the resulting supernatant was labelled sample "M", and the precipitate, redispersed in 10 mL of toluene, sample "L". The resulting average edge sizes for samples S, M and L are respectively 9 ± 1, 11 ± 1 and 16 ± 3 nm, to be compared with the 12 ± 3 nm average size of the pristine sample (S1).

Surface chemical treatments. The surface treatments were performed by preparing a soy-lecithin capped nanocrystal dispersion of known concentration and dividing it into different flasks. Then, increasing amounts of the new ligand were mixed with these dispersions at ambient conditions, exploring increasing ligand-to-lecithin ratios. The mixtures were then stored at ambient conditions without further manipulations.

Characterizations

Optical characterizations. UV-Vis absorption spectra, photoluminescence (PL) spectra and quantum yields (PLQY) of the colloidal dispersions were obtained using an FS5 spectrofluorometer (Edinburgh Instruments). Absorption spectra were obtained in transmission mode. Photoluminescence spectra were recorded at an excitation wavelength of 350 nm, an integration time of 100 ms per data point, and a spectral resolution of 1 nm. PLQY were obtained at an excitation wavelength of 365 nm, an integration time of 100 ms per data point, and a spectral resolution of 0.4 nm.

Transmission electron microscopy (TEM). TEM images were acquired on a JEOL JEM-2100 TEM equipped with a LaB_6 electron source, operating at 200 kV.

Powder X-ray diffraction (PXRD). Diffractograms were acquired on a MalvernPanalytical Aeris diffractometer equipped with a copper Kα anode. Samples were prepared by drying the colloidal dispersions on a low-background silicon substrate.

Radioluminescence and photoluminescence. On a 5 × 5 mm^2 Si wafer, volumes of samples giving a final thickness of about 0.5 μm were deposited and let dry. The radio/photoluminescence spectroscopy setup consists of an X-ray tube, a samples holder, a monochromator and a CCD. Additionally, a LED emitting at λ = 405 nm can be used in order to obtain the PL spectrum in the very same conditions as the RL one, which greatly facilitates the comparison. The luminescence time decays' setup consists of a pulsed laser emitting at 405 nm (HORIBA DDL405), a monochromator, a photomultiplier tube (PMT), the PicoHarp300 time-correlated single photon counting (TCSPC) and several filters. Time-resolved emission spectra under X-ray excitation are obtained using a pulsed laser DeltaDiode-405L from Horiba emitting at 405 nm hitting the photocathode of an X-ray tube from Hamamatsu (N5084) set at 35 kV. Emitted light was collected using a monochromator from Andor (Kymera 193i) with a grating of 300 lines per mm. Detection is performed using a hybrid photomultiplier tube (HPM 100-40c) from Becker & Hickl GmbH.

Compton-TDCR. Triple to double coincidence ratio measurements were obtained with a Compton-TDCR system equipped with a gamma spectrometer designed and developed at LNE-LNHB.[39] Briefly, the development of a Compton coincidence measurement system involves the utilization of an external collimated mono-energetic gamma-ray source, as depicted in Fig. 1d. This source directly interacts with an energy E within the scintillator. A gamma-ray detector positioned at a specific angle relative to the source beam is used to measure the Compton-scattered photons with energy E' within the scintillator. When these scattered photons are detected in coincidence with the light photons emitted by the scintillator, the scintillation efficiency can be derived as a function of the energy of the interacting electrons.

Results and discussion

Commercial liquid scintillators are traditionally multi-component organic solutions, usually involving an organic dye as the light-emitter, a wavelength shifter which helps to maximize the light detection by the photodetectors, some surfactant stabilizing agents and of course a solvent. Their scintillation pro-

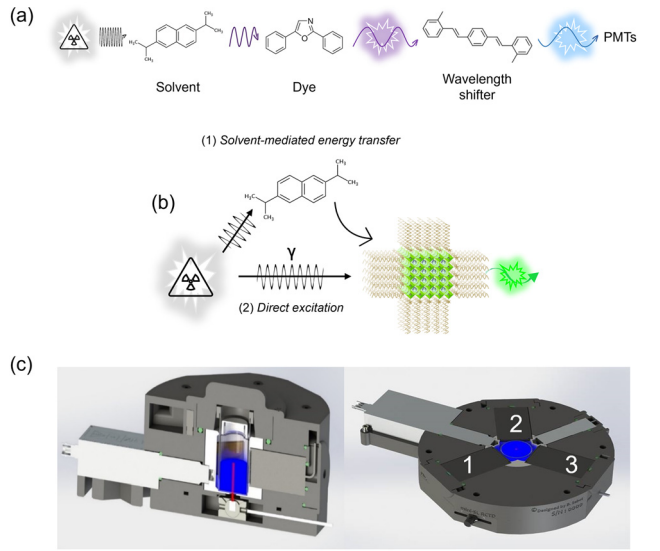

Fig. 1 Schematic representations of the energy transfer processes involved in liquid scintillation: (a) example of a traditional organic scintillator DIPN (diisopropylnaphtalene) as the solvent, PPO (2,5-diphenyloxazole) as the dye and bis-MSB [*p*-bis-(*o*-methylstyryl)-benzene] as the wavelength shifter. (b) and (c) Possible liquid scintillation mechanisms in the case of solvent/PNC mixtures. (d) Compton-TDCR setup scheme: on the left, the three PMTs around the sample are highlighted (1, 2 and 3), and on the right a section of the setup is shown, highlighting the Am-241 source located under the sample.

cesses work on the basis of energy transfers (scheme in Fig. 1a): it starts with the organic solvent, which is by definition the main component of the mixture and thus has the highest probability of interaction with the ionizing radiation, which comes from a radioactive sample dissolved in the mixture or from an external instrumental source. The impacted solvent molecules pass to a highly excited state, and then interact with dye molecules, usually through non-radiative processes, transferring to them their excitation energy. The now excited organic dye relaxes to its ground-level state through a radiative emission, which is absorbed by the wavelength shifter which is then meant to re-emit a radiation which better matches the maximum detection efficiency of the photodetectors. The number of steps involved in these processes and their overall rate, together with their already mentioned low density, leave room for possible improvements of these liquid scintillation systems. This whole energy deposition pathway is also rather complex in terms of modelling, adding uncertainties when metrology uses are targeted.

To simplify the nanocrystals liquid scintillator as much as possible and directly study the energy deposition pathways between the solvent and the PNCs, it was decided to remove molecular intermediates and to directly study the system presented in Fig. 1b, composing of PNC directly dispersed in a usual liquid scintillation solvent: 2,6-diisopropylnaphthalene. This solvent has the advantage of being not volatile, possesses a low toxicity, and is an effective dispersion medium for PNCs due to its low polarity. In this binary mixture, the possible energy deposition pathways are different than in the former organic scintillator case. Indeed, the primary interaction can now also occur in the PNC, taking advantage of its high density and high γ-rays or X-rays stopping power.

The characterization of these interactions and the colloidal $CsPbBr_3$ nanocrystal scintillating performances in liquid scintillation conditions was done using a recently developed experiment called Compton-TDCR (Triple-to-Double Coincidence Ratio). This experiment is fully detailed in ref. 44. The general idea is to correlate the detection of scintillation photons with the energy of detected secondary γ-rays to be able to characterize the energy deposition mechanisms in the scintillating liquid. Indeed, the main interaction pathway of an incident γ-ray with the liquid scintillator is through Compton effect, *i.e.* elastic scattering of the γ photon by electrons, creating photoelectrons and a lower energy γ-photon. This experimental setup involves three photomultipliers (PMTs) positioned all around the sample to detect the scintillation, together with an X-gamma spectrometer (here a CdTe semiconductor), and a sealed ^{241}Am source placed under the liquid scintillation vial (Fig. 1d). The monochromatic γ-rays emitted by the source at 59.6 keV interact with the sample mainly by Compton effect, thus inducing photoelectrons that interact with the liquid medium depositing energy and causing the above described chain of energy transfers, and finally the light emission. Each generated photo-electron interacting with the liquid scintillator induces the emission of numerous visible photons, depending on its energy.

The measurement involves detecting coincidences of light photons in the three PMTs. In this setup, the signals collected by a single PMT only (no coincidences), are treated as either PMT noise or indication of low signal, potentially due to self-absorption phenomena. These phenomena occur when some photons emitted during an event are unable to cross the liquid medium and reach more distant PMTs. On the other hand, double coincidences (D) are considered reliably detected events (as they discard the noise) and are a measure of the number of emissive events that occurred during the scintillation process. Additionally, the triple coincidences (T) are considered, though the ratio T/D, as an indicator of the number of emitted photons of those emissive events. From these considerations and from the setup's geometry, the T/D factor, the triple to double coincidence ratio, is mathematically linked to the scintillation yield.

In detail, the ratio T/D is related to the mean number of detected photons leading to photoelectrons (n_{pe}) per event. n_{pe} determined by the TDCR method[45] is called the scintillation yield when the initial energy is known. From the Compton-TDCR method, the γ-ray detector is adapted to detect the Compton scattered γ-rays as well as the X-ray fluorescence photons in coincidence with the T/D ratio. As a result, if T/D is measured in coincidence with a detected event in the γ channel, the deduced n_{pe} corresponds to a known kinetic energy of the electron interacting in the scintillator and producing light. A detailed understanding emerges when plotting D or n_{pe} as a function of the deposited electron energy. It is essential to emphasize that D and T/D encompass distinct information. D indicates the count of detected events per second, representing detection efficiency. This parameter depends on the density, the scintillation yield, and the deposited energy. T/D and consequently n_{pe} represent the mean number of detected photons produced per event. When plotted as a function of the deposited energy, it allows to estimate the number of detected photons per deposited keV. When obtained on the entire γ-ray spectrum, it gives the number of detected photons for the average deposited energy.

The use of this unique Compton-TDCR setup aims to facilitate the assessment and comparison of different colloidal $CsPbBr_3$ nanocrystal mixtures. This intention is an attempt to decipher the scintillation mechanism and the factors influencing it in this case of PNCs dispersed in a liquid matrix. The liquid scintillation process encompasses a complex cascade of events where numerous parameters play a role, including PNC concentration, fluorescence quantum efficiency, average size and surface stabilizing ligands.

Consequently, selecting the appropriate composition of the PNC scintillating mixtures to study demands careful consideration. First, the colloidal stability of the dispersions is of utmost importance in order to increase the PNCs loading – thus the mixture's density- and to perform the TCDR due to the measurement duration (up to several days for the Compton TDCR measurements). The colloidal dispersion concentration is a second crucial parameter in liquid scintillation, since higher concentrations will increase the probability of ionizing

radiation interaction with the PNCs and thus the system's efficiency. It may also affect the potential probability of energy transfer from the solvent to the NC. On the other hand, these semiconductor nanocrystals suffer from a short Stokes shift, implying that excessive loading will lead to self-absorption of the emitted light. Other essential factors are light production and collection. For the former, the samples must show high photoluminescence quantum yields (PLQYs), high intrinsic scintillation quantum yield and a good solvent-to-nanoparticles energy transfer efficiency, where the nanocrystals stabilizing ligands would play a critical role. The efficient light collection is subjected to the light self-absorption, which can be partly mitigated by drastically improving the PLQY (by repairing the surface defects). To a smaller extent, it is also subjected to the light emission decay time, since the TCDR technique is based on a coincidence method, and this is also improvable by repairing the surface defects.

These different considerations led to the choice of soy lecithin-capped PNCs, since this zwitterionic capping ligand has been shown to allow the synthesis of highly colloidally stable dispersions even at concentrations as high as 400 mg mL^{-1}.[42] Such stability offers the advantage of exploring the PNC dispersion scintillation properties at different concentrations in order to evaluate their efficiency and the self-absorption influence.

The synthesis was modified from the original published protocol to increase PNC production by a factor of five.[42] The obtained perovskite nanocrystals are illustrated by a TEM picture in Fig. 2a, highlighting their polydispersity in size (12 ± 3 nm). This polydispersity allowed us to isolate different-sized populations through size selective precipitation in order to study the influence of this parameter on the liquid scintillation performance. Fig. 2 shows comparisons between the pristine sample, polydisperse, and the smallest size fraction obtained by selective precipitation (additional characterizations for the other sized fractions are available in ESI†). The TEM image Fig. 2b corresponds to this smallest fraction with an average PNC edge of 9 ± 1 nm. The absorption spectrum (Fig. 2c) highlight a better resolution of the excitonic features from pristine to the small (S) fraction, induced by a decrease of polydispersity. A slight blue shift in absorption and photoluminescence spectra is also observed when decreasing the PNCs' average size, consistently with quantum confinement effect. The XRD patterns (Fig. 2e) are characteristic of the orthorhombic phase, and further evidence the size decreases with an enlargement of the peaks for the small-size sample. A first set of scintillation characterizations was acquired on PNCs thin films obtained by drop casting (to limit self-absorption phenomena), consisting of radioluminescence spectra (Fig. 2d) and radioluminescence time decays (Fig. 2f). The emission spectra obtained under X-ray excitation (*i.e.* radioluminescence spectra) confirm that these soy-lecithin PNC are scintillating efficiently. The luminescence behavior differences between photoluminescence and radioluminescence thin film measurements on the small "S" sample and the "pristine" polydisperse sample can be qualitatively described as follows: photoluminescence excitation only excite the surface of the PNC film whereas the X-rays homogeneously excite the whole film. The RL emission is then red-shifted compared to the PL emission through reabsorption and photon recycling effects. The effect is more pronounced on the "pristine" polydisperse sample where bluer emission arising from smaller PNC can be efficiently reabsorbed by the bigger redder PNC in the film.

The scintillation time decays demonstrate further that these PNCs are fast scintillators, and this property is not affected by the nanoparticle size, the lifetimes being in the order of 1 ns for each sample. This behaviour can be related to the similar measured fluorescence quantum yields of these two PNC samples, of about 25% for both.

A preliminary set of TDCR measurements was conducted on PNC samples with increasing concentrations. The results indicated that increasing the concentration massively degrades the scintillation performances, as evidenced by the drop of double coincidences D (see Fig. S6†). This was interpreted as evidence that the vast majority of photons produced during the scintillation process don't reach the detectors before being reabsorbed by the medium, and that the T/D values increase artificially only because D tends to zero. The concentration chosen for further study was 0.06 mg mL^{-1}, corresponding to an optical density at the first exciton of 0.2. This concentration demonstrates an encouraging amount of emitted photons, coupled with the highest apparent photoluminescence quantum yield, consistent with a less impact on self-absorption (Fig. S6†). A second set of TDCR measurement was then conducted on PNC samples with increasing average sizes. No significant difference in their performances was measured, with just a slight enhancement in the case of the smallest sizes (Fig. S7†).

The initial problems faced during the TDCR measurements pointed luminescence quantum efficiency as a crucial parameter to optimize, and this can be tuned by PNC surface engineering. As previously stated, the advantage of using soy lecithin as the stabilizing ligand, a long and quite bulky zwitterionic molecule (see sketch Fig. S8†) that strongly binds to the PNCs surfaces, is that it allows to obtain colloidally stable dispersions, a crucial factor for increasing the nanoparticles loading in the liquid mixture. On the other hand, such a big and bulky molecule can inhibit the energy transfers from the excited organic solvent to the PNCs during the energy relaxation and transfer process, and moreover, the obtained PNC photoluminescence quantum yields don't exceed 50%. Consequently, different kinds of organic molecules were tested in surface treatment experiments. The addition of new ligands can potentially have two benefits: an increase of PLQY by repairing the surface defects,[46,47] and – in the case of shorter and electronically delocalized molecules – an increase of energy transfers between solvents and PNCs. Fig. 3a presents the list of the most relevant tested molecules (complete list in Fig. S9†), and includes different kinds of organic systems containing various functional groups: ammonium bromides, that can interact with lead and bromide vacancies,[11,48–50] and carboxylic acids, which have affinity for lead-rich surfaces.[51]

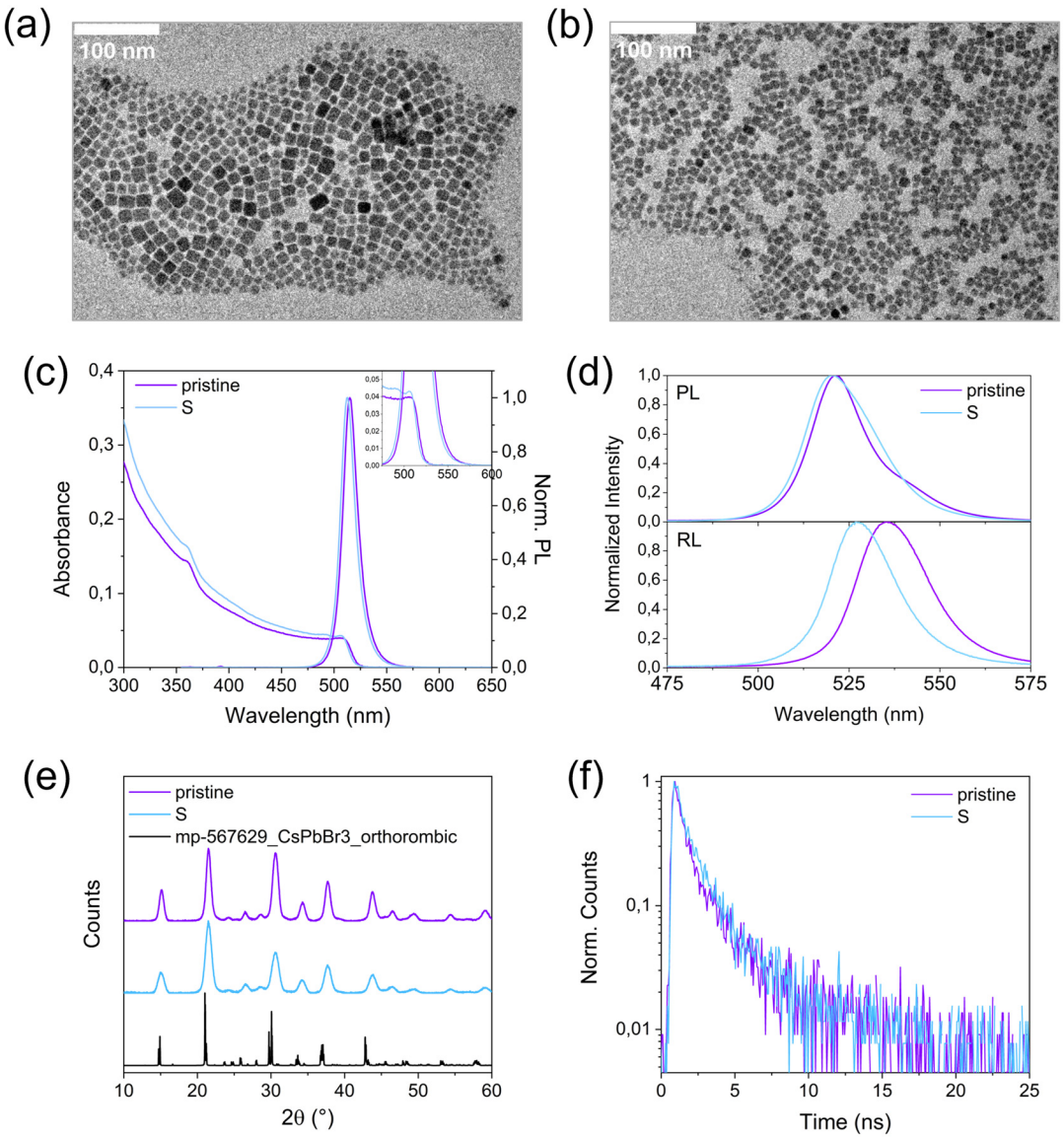

Fig. 2 TEM images of the pristine, polydisperse $CsPbBr_3$ sample (a) and of the smallest "S" fraction (b); absorption and photoluminescence (λ_{exc} = 365 nm) spectra of the polydisperse "pristine" and smallest "S" fraction samples in solution (c); photo- and radioluminescence spectra of the polydisperse "pristine" and smallest fraction "S" samples dried over Si wafers (d); XRD patterns of the polydisperse "pristine" and smallest "S" fraction samples, compared to the reference pattern for a $CsPbBr_3$ orthorombic structure (e); radioluminescence time decay of the polydisperse "pristine" and smallest "S" fraction samples (f).

Hexylammonium bromide was initially chosen as representative of non-conjugated ammonium bromide salt. In contrast, the other selected molecules are conjugated systems, since this feature – involving electronic wavefunctions delocalized over the whole structure – was thought to possibly be more efficient in coupling with the organic solvent and thus allowing non-radiative energy transfers to the inorganic PNCs. Phenethylammonium bromide stands in between both behaviours, the conjugated part being separated from the ammonium binding moiety.

The surface treatment protocol is detailed in the Experimental section, and briefly consists in the introduction of a variable amount of new ligands. Changes were monitored through optical measurements (absorbance and luminescence). Fig. 3e shows the influence of three different kinds of chemical functions on the PLQY (photographs of the samples Fig. 3b and c). A general increment of the PLQY is observed as a function of the addition of the new chemical in the mixture in the case of phenethylammonium bromide (PEABr) and hexylammonium benzoate (HAB), whereas benzoic acid (BA) alone doesn't cause any remarkable improvement. As such an ammonium salt was considered more efficient in this case for repairing the PNC surface defects by passivating bromide and lead surface vacancies. In particular, the test that was considered the most successful was the one involving hexylammonium benzoate, even though the absorption spectra in Fig. 3d

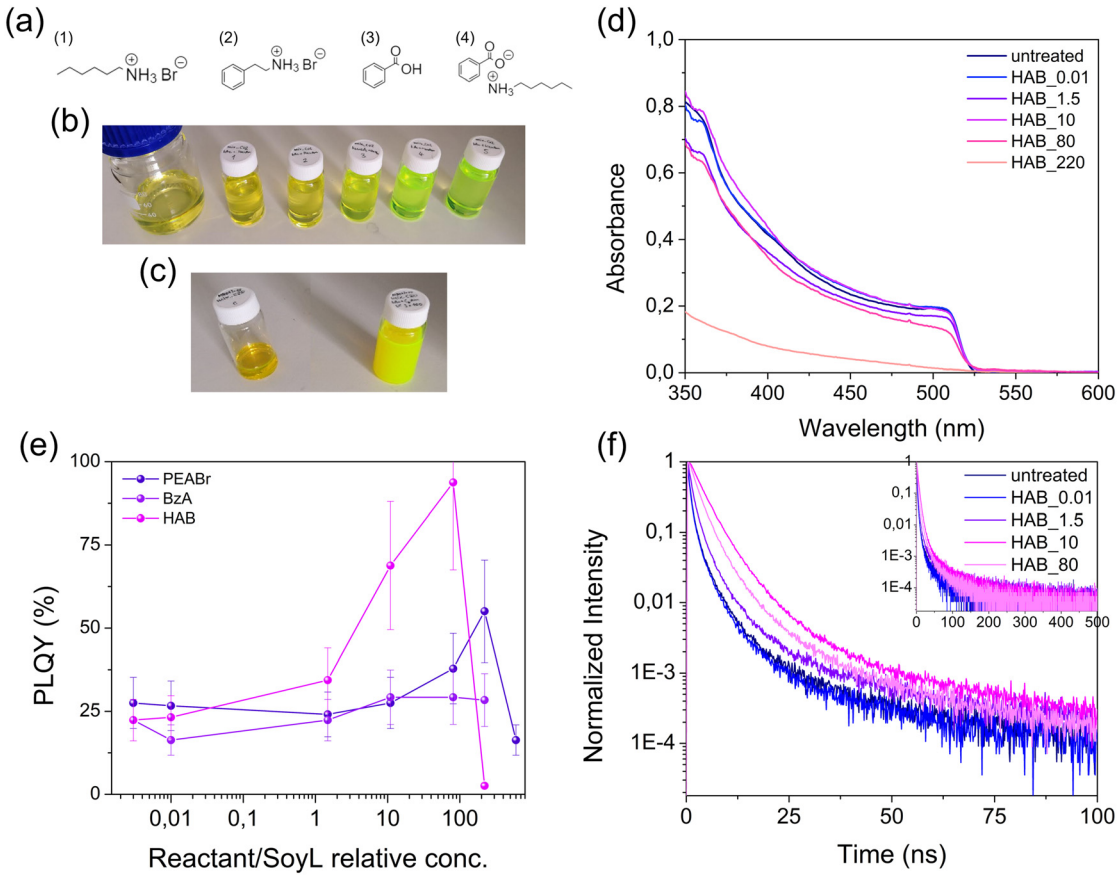

Fig. 3 Chemical structures of hexylammonium bromide (1), phenethylammonium bromide (2), benzoic acid (3), hexylammonium benzoate (4) (a); picture of the HAB chemical treatment series in the 0.056 mg mL^{-1} concentration in daylight (b); picture of the HAB chemical treatment series in the 5.6 mg mL^{-1} concentration in daylight (c); absorption spectra of the PNCs treated with hexylammonium benzoate (HAB), at increasing HAB/soy lecithin relative concentration (d); photoluminescence quantum yield of chemically treated samples as a function of increasing amounts of added chemical, at excitation λ = 365 nm (e); PL time decay of hexylammonium benzoate treated samples at increasing HAB/soy lecithin relative concentration, at an excitation λ = 440 nm (f).

show a degradation of the optical absorption for the samples with a HAB to surface soy lecithin ratio higher than 10. The latter was then considered as the most promising sample in terms of PLQY (about 80%) and stability.

Another evidence of the improved PNCs' PLQY is their PL decay profiles shown in Fig. 3f, where the PNCs apparent lifetime increases with the increase of ligands concentration, thus indicating a reduction in the number of surface defects. Surprisingly, FTIR experiments conducted on the nanocrystals before and after the surface defects treatment (see Fig. S11†) do not show noticeable changes in the infrared spectra. We can then conclude that the passivation effect induced by the chemical treatments does not strongly modify the overall stabilizing ligands chemistry, which is consistent with the maintained optimal colloidal stability of the samples.

These treated samples were then tested using Compton-TDCR measurements, in order to investigate their behaviour during the scintillation process. As described above, the phenomenon of scintillation may occur through several paths depending on the primary interaction's location. If the initial γ-ray interaction occurs in the solvent, then resultant electron excites the solvent and an energy transfer from the solvent to the PNC is required to obtain the emission of light as for traditional liquid scintillators (Fig. 1b). Conversely, if the primary interaction occurs in the PNC, then part of the energy of the generated electron may deposit in the PNC, thereby generate light (Fig. 1c). In this case, X-ray fluorescence may also occur and the XK-Line of caesium and XL-line of lead may be detected in the γ-ray spectrum. This occurrence is visible in Fig. S13,† wherein these lines are clearly identified when the liquid is loaded with PNCs at high concentrations.

A first step, represented Fig. 4a, was to plot for a wide range of treated samples having different surface chemistries, concentrations and fluorescence QY, the evolution of the scintillation yield as a function of the PNC PLQY. The blue groups of points correspond to PNC treated with different concentrations of PEABr and benzoic acid and thus exhibiting different PLQY. On the other hand, the yellow, orange and red points correspond to high PLQY PNCs samples obtained with optimum hexylammonium benzoate (HAB) ligands but with different PNC concentrations.

This first result that can be extracted from Fig. 4a, is the correlation between the optical quantum yield and the average

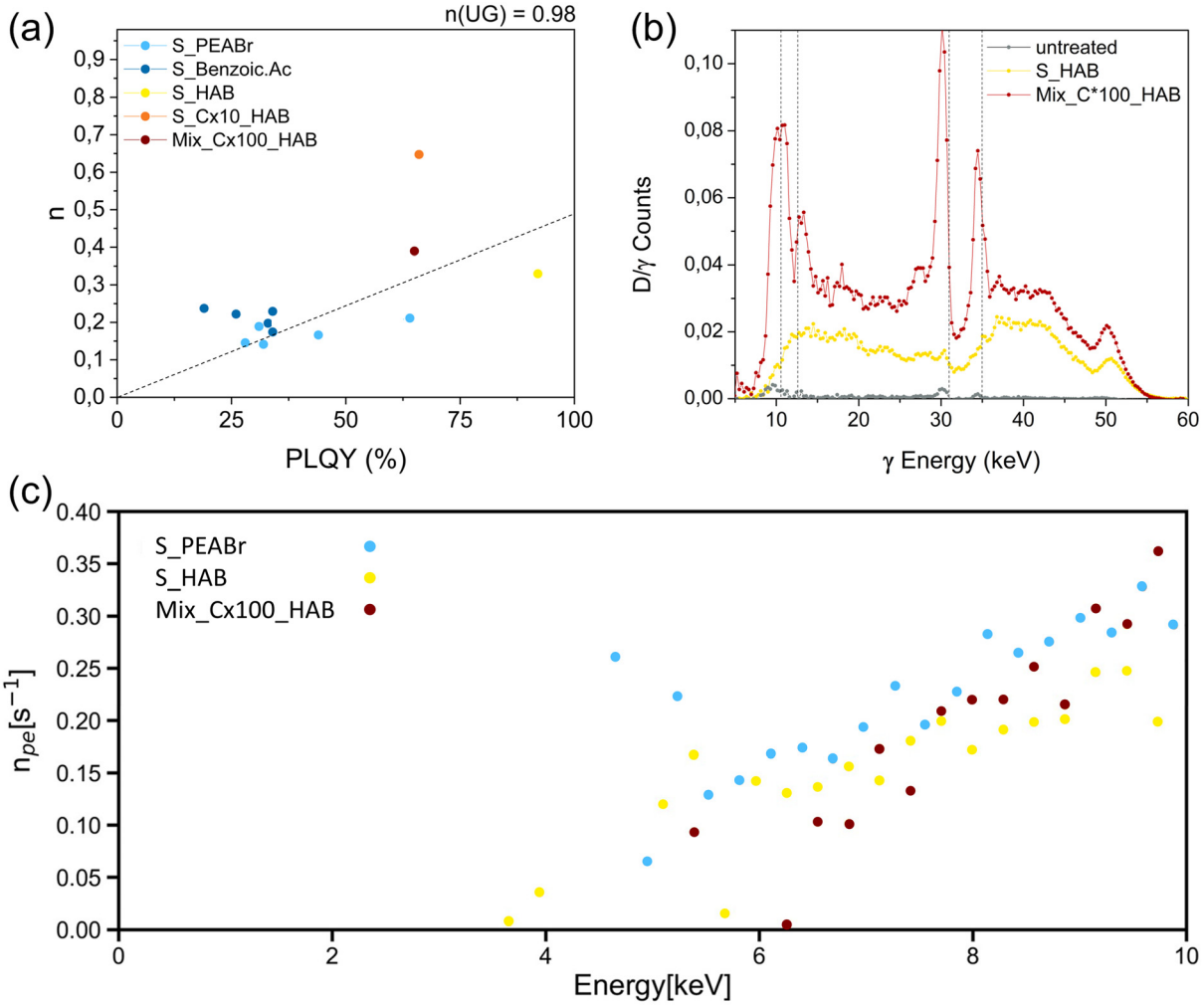

Fig. 4 n_{pe} values of treated samples as a function of the ligand surface treatment-induced PLQY enhancement, the dashed line is a guideline only (a); compton-TDCR spectra obtained by measuring the coincidence between gamma and D channel (light detector) (b); scintillation non proportionality curves obtained with the Compton-TDCR experiment in the range of 3 keV to 10 keV electron energy deposited in the material (c). The dotted lines correspond to X-rays emission thresholds for Lead (Pb Lα1 = 10.55 keV, Pb Lβ1 = 12.61 keV) and Caesium (Cs Kα = 30.97 keV, Cs Kβ = 34.98 keV).

n_{pe}. Since the luminescence mechanism corresponds to the last stage of the scintillation process, the significance of the optical quantum yield is convincingly demonstrated. This pertains to the correlation between n_{pe} with surface treated and untreated particles, with the same concentration. Additionally, the concentration exhibits a double role. Elevating the concentration by a factor of 10 increases n_{pe}, whereas a 100-fold increase in concentration decreases the average n_{pe}. This decrease at high concentrations unequivocally indicates the self-absorption effect due to the strong overlap between the emission and the absorption spectrum (Fig. 2c), as frequently observed in direct band gap semiconductors. In these conditions, the best liquid scintillator we obtained is then the orange dot, corresponding to the small fraction PNC at 10 times their initial concentration (and then to an optical density of 2 at the first exciton) and treated with HAB ligands.

The increase in the average n_{pe} requires careful analysis. As previously elucidated, such an increase may be due to an increase in the intrinsic scintillation yield or to a variation in the mean deposited energy, which is clearly seen in Fig. S13.† Fig. 4c illustrates the n_{pe} as a function of the electron energy for S_PEABr (blue), S_HAB (yellow) and Mix_HAB Cx100 (dark red). The spectrum is restricted to the range below 10 keV due to potential perturbations arising from double Compton events at higher energies. Low and high concentration samples HAB treated exhibit almost the same scintillation yield of about 0.045 ± 0.005 photoelectron per keV. This highlights that within the concentration range, augmenting concentrations do not modify intrinsic scintillation yield, implying that the increase observed in Fig. 4a can be attributed to a change in the mean deposited energy.

The main effect of the PNC treatment and concentration occurs when considering the detection efficiency (D). Fig. 4b presents the spectrum of D when considered in coincidence with the γ-ray channel for untreated high-concentration PNC sample (green) and treated HAB sample at low concentration

(S_HAB, purple) and concentrated one hundredfold (S_HAB Cx100, orange). The comparison between untreated and treated samples at the same concentration, then with the same interaction probability, reveals the effect on the increase of the PL quantum yield leading to the increase of the intrinsic scintillation yield. The average n_{pe} per keV is significantly low, leading to a marginal probability of achieving a double coincidence. Comparing the D spectrum between S_HAB and S_HAB Cx100 highlights the influence of the stopping power, signifying a heightened likelihood of γ-ray interaction with the liquid when highly loaded with nano-scintillating perovskite.

The observed lines in Fig. 4b correspond to the X-ray fluorescence lines of caesium and lead, thus indicating the situation where the primary interaction occurs in the PNC. Notably, D is multiplied by a factor from 5 to 8 while the PNC concentration is increased tenfold. This confirms that the dominating scintillating mechanism is the direct energy deposition in PNCs rather than an energy transfer from the solvent to the nanocrystal. It also underscores the crucial role of the stopping power when the liquid is loaded and that strategies enabling higher concentration without self-absorption could further enhance overall efficiency. For example, adding another wavelength-shifter could be a successful strategy, as demonstrated for plastic scintillators.[26,52]

Finally, it is remarkable that these samples reach a n_{pe} value which is close to the one for UltimaGold® liquid scintillator standard, represented by the graph's upper limit, but with a PMTs setup which is 2.4 less sensitive to this work's samples emission wavelength (Fig. S14†), and with solutions that are about two orders of magnitude less concentrated.

Conclusion

We have presented a study on the behaviour of colloidal perovskite $CsPbBr_3$ nanocrystals as liquid scintillators. Treated with chemicals of different nature in order to repair the surface defects, their PLQY then their scintillating performances have been greatly improved. In particular, the surface treatment with hexylammonium benzoate made it possible to obtain an average number of photons detected per emissive event which is comparable to the used reference the Ultima Gold organic liquid scintillator.

A Compton-TDCR experiment was then used to finely characterize the energy deposition processes in these solvent/PNC binary mixtures. We demonstrated that – contrarely to traditional organic liquid scintillators where the energy is majoritarely deposited in the solvent – perovskite nanocrystals themselves are the main locii of energy deposition. This is most likely due to the high density of the nanocrystals and the presence of heavy elements such as lead and caesium. PNCs have then a double role as liquid scintillators, being at the same time energy deposition centres and visible light emitters.

These results can be readily extended to the more general case of composite materials comprising nanocrystals and improve our understanding of the use of nanocrystals for scintillation. They further pave the way for the development of new technologies for liquid scintillation cocktails, either comprising nanocrystal emitting centers or nanocrystals as γ absorbers, or both.

Author contributions

All authors contributed to the design of experiments, interpretation of the results and discussion of the outline of the manuscript. B. M., B. S. and C. D. supervised the project, M. B. performed the syntheses and structural characterisations, B. S. carried out the TDCR measurements, M. B., C. D. and B. M. wrote the manuscript.

Data availability

The data supporting this article have been included as part of the ESI.†

Conflicts of interest

The authors declare that they have no known competing financial interests or personal relationships that could have appeared to influence the work reported in this paper.

Acknowledgements

B. M. thanks the Université de Lyon PALSE program under the framework "Investissements d'avenir" (ANR-11-IDEX-0007). B. S. Thanks the Laboratoire National de Métrologie et d'Essais (LNE) for the funding in the framework of SCINTIPLUS project. F. M. and C. D. acknowledge the financial support from the Ministry of Education, Singapore, under its AcRF Tier 2 grant (MOE-T2EP50121-0012) and AcRF Tier 1 grant (RG140/23).

References

1 Q. A. Akkerman, G. Rainò, M. V. Kovalenko and L. Manna, Genesis, challenges and opportunities for colloidal lead halide perovskite nanocrystals, *Nat. Mater.*, 2018, **17**, 394–405.
2 C. Cueto, C. Donoghue, K. Bolduc and T. Emrick, Zwitterionic Block Copolymers for the Synthesis and Stabilization of Perovskite Nanocrystals, *Chem. – Eur. J.*, 2022, **28**, 2071–2083.
3 A. Dey, *et al.*, State of the Art and Prospects for Halide Perovskite Nanocrystals, *ACS Nano*, 2021, **15**, 10775–10981.
4 L. Polavarapu, B. Nickel, J. Feldmann and A. S. Urban, Advances in Quantum-Confined Perovskite Nanocrystals for Optoelectronics, *Adv. Energy Mater.*, 2017, **7**, 1–9.

5 C. C. Stoumpos and M. G. Kanatzidis, Halide Perovskites: Poor Man's High-Performance Semiconductors, *Adv. Mater.*, 2016, **28**(28), 5778–5793.
6 C. C. Stoumpos and M. G. Kanatzidis, The Renaissance of Halide Perovskites and Their Evolution as Emerging Semiconductors, *Acc. Chem. Res.*, 2015, **48**, 2791–2802.
7 M. C. Weidman, A. J. Goodman and W. A. Tisdale, Colloidal Halide Perovskite Nanoplatelets: An Exciting New Class of Semiconductor Nanomaterials, *Chem. Mater.*, 2017, **29**, 5019–5030.
8 L. Protesescu, *et al.*, Nanocrystals of Cesium Lead Halide Perovskites (CsPbX 3, X = Cl, Br, and I): Novel Optoelectronic Materials Showing Bright Emission with Wide Color Gamut, *Nano Lett.*, 2015, **15**, 3692–3696.
9 J. Shamsi, A. S. Urban, M. Imran, L. De Trizio and L. Manna, Metal Halide Perovskite Nanocrystals: Synthesis, Post-Synthesis Modifications, and Their Optical Properties, *Chem. Rev.*, 2019, **119**, 3296–3348.
10 G. F. Knoll, *Radiation Detection and Measurement*, 4th edn, 2010.
11 W. Chen, *et al.*, Surface–Passivated Cesium Lead Halide Perovskite Quantum Dots: Toward Efficient Light–Emitting Diodes with an Inverted Sandwich Structure, *Adv. Opt. Mater.*, 2018, **6**, 1800007.
12 Q. Chen, *et al.*, All-inorganic perovskite nanocrystal scintillators, *Nature*, 2018, **561**, 88–93.
13 Y. Zhang, *et al.*, Metal Halide Perovskite Nanosheet for X-ray High-Resolution Scintillation Imaging Screens, *ACS Nano*, 2019, **13**(2), 2520–2525.
14 F. Maddalena, *et al.*, Inorganic, Organic, and Perovskite Halides with Nanotechnology for High–Light Yield X- and γ-ray Scintillators, *Crystals*, 2019, **9**, 88.
15 H. Wei and J. Huang, Halide lead perovskites for ionizing radiation detection, *Nat. Commun.*, 2019, **10**, 1066.
16 Y. C. Kim, *et al.*, Printable organometallic perovskite enables large-area, low-dose X-ray imaging, *Nature*, 2017, **550**, 87–91.
17 W. Zhu, *et al.*, Low-dose real-time X-ray imaging with non-toxic double perovskite scintillators, *Light: Sci. Appl.*, 2020, **9**, 112.
18 A. Jana, *et al.*, Perovskite: Scintillators, direct detectors, and X-ray imagers, *Mater. Today*, 2022, **55**, 110–136.
19 S. Li, *et al.*, Review: Perovskite X-ray Detectors (1997–Present), *Crystals*, 2022, **12**, 1563.
20 H. Chen, Y. Li, B. Zhao, J. Ming and D. Xue, Nanocrystals of metal halide perovskites and their analogues as scintillators for x-ray detection, *Nano Futures*, 2022, **6**, 012001.
21 J. H. Heo, *et al.*, High–Performance Next–Generation Perovskite Nanocrystal Scintillator for Nondestructive X–Ray Imaging, *Adv. Mater.*, 2018, **30**, 1–6.
22 C. Dujardin, *et al.*, Needs, Trends, and Advances in Inorganic Scintillators, *IEEE Trans. Nucl. Sci.*, 2018, **65**, 1977–1997.
23 X. Xu, *et al.*, Halide perovskites: A dark horse for direct X–ray imaging, *EcoMat*, 2020, **2**(4), e12064.
24 F. Maddalena, *et al.*, Stable and Bright Commercial $CsPbBr_3$ Quantum Dot-Resin Layers for Apparent X-ray Imaging Screen, *ACS Appl. Mater. Interfaces*, 2021, **13**, 59450–59459.
25 M. D. Birowosuto, *et al.*, X-ray Scintillation in Lead Halide Perovskite Crystals, *Sci. Rep.*, 2016, **6**, 37254.
26 M. Gandini, *et al.*, Efficient, fast and reabsorption-free perovskite nanocrystal-based sensitized plastic scintillators, *Nat. Nanotechnol.*, 2020, **15**, 462–468.
27 Y. Zhou, J. Chen, O. M. Bakr and O. F. Mohammed, Metal Halide Perovskites for X-ray Imaging Scintillators and Detectors, *ACS Energy Lett.*, 2021, **6**, 739–768.
28 A. Abusleme, *et al.*, Optimization of the JUNO liquid scintillator composition using a Daya Bay antineutrino detector, *Nucl. Instrum. Methods Phys. Res., Sect. A*, 2021, **988**, 164823.
29 P. Cassette, *Mesures de radioactivité par scintillation liquide*, Tech. d'analyse, 2020. DOI: **10.51257/a-v2-p2552**.
30 I. A. Suslov, *et al.*, Development of a new tellurium loaded liquid scintillator based on linear alkylbenzene, *Nucl. Instrum. Methods Phys. Res., Sect. A*, 2022, **1040**, 167131.
31 Y. J. Zhu and D. Z. Yang, The use of liquid scintillation analysis in the monitoring of α emitting and transuranium nuclides in environmental samples, *J. Radioanal. Nucl. Chem. Artic.*, 1995, **194**, 173–175.
32 J. D. Davidson and P. Feigelson, Practical aspects of internal-sample liquid scintillation counting, *Int. J. Appl. Radiat. Isot.*, 1957, **2**, 1–18.
33 B. J. Land, *et al.*, MeV-scale performance of water-based and pure liquid scintillator detectors, *Phys. Rev. D*, 2021, **103**, 052004.
34 E. Rapkin, Liquid scintillation counting 1957–1963: A review, *Int. J. Appl. Radiat. Isot.*, 1964, **15**, 69–87.
35 Q. Xu, *et al.*, Lead halide perovskite quantum dots based liquid scintillator for x-ray detection, *Nanotechnology*, 2021, **32**, 205201.
36 S. Cho, *et al.*, Hybridisation of perovskite nanocrystals with organic molecules for highly efficient liquid scintillators, *Light: Sci. Appl.*, 2020, **9**, 156.
37 H. Yu, T. Chen, Z. Han, J. Fan and Q. Pei, Liquid Scintillators Loaded with up to 40 Weight Percent Cesium Lead Bromide Quantum Dots for Gamma Scintillation, *ACS Appl. Nano Mater.*, 2022, **5**, 14572–14581.
38 E. Graham, *et al.*, Light yield of Perovskite nanocrystal-doped liquid scintillator, *J. Instrum.*, 2019, **14**, P11024.
39 B. Sabot, C. Dutsov, P. Cassette and K. Mitev, Performance of portable TDCR systems developed at LNE-LNHB, *Nucl. Instrum. Methods Phys. Res., Sect. A*, 2022, **1034**, 166721.
40 R. Broda, A review of the triple-to-double coincidence ratio (TDCR) method for standardizing radionuclides, *Appl. Radiat. Isot.*, 2003, **58**, 585–594.
41 A.-L. Bulin, *et al.*, Modelling energy deposition in nanoscintillators to predict the efficiency of the X-ray-induced photodynamic effect, *Nanoscale*, 2015, **7**, 5744–5751.
42 F. Krieg, *et al.*, Stable Ultraconcentrated and Ultradilute Colloids of CsPbX 3 (X = Cl, Br) Nanocrystals Using Natural Lecithin as a Capping Ligand, *J. Am. Chem. Soc.*, 2019, **141**, 19839–19849.

43 J. De Roo, *et al.*, Highly Dynamic Ligand Binding and Light Absorption Coefficient of Cesium Lead Bromide Perovskite Nanocrystals, *ACS Nano*, 2016, **10**(2), 2071–2081.
44 B. Sabot, *et al.*, A compact detector system for simultaneous measurements of the light yield non-linearity and timing properties of scintillators, *Sci. Rep.*, 2024, **14**, 1–19.
45 J. D. Valentine and B. D. Rooney, Design of a Compton spectrometer experiment for studying scintillator non-linearity and intrinsic energy resolution, *Nucl. Instrum. Methods Phys. Res., Sect. A*, 1994, **353**, 37–40.
46 J. Ye, *et al.*, Defect Passivation in Lead–Halide Perovskite Nanocrystals and Thin Films: Toward Efficient LEDs and Solar Cells, *Angew. Chem.*, 2021, **133**, 21804–21828.
47 Y. Bai, M. Hao, S. Ding, P. Chen and L. Wang, Surface Chemistry Engineering of Perovskite Quantum Dots: Strategies, Applications, and Perspectives, *Adv. Mater.*, 2022, **34**(4), 2105958.
48 M. Imran, *et al.*, Simultaneous Cationic and Anionic Ligand Exchange For Colloidally Stable CsPbBr 3 Nanocrystals, *ACS Energy Lett.*, 2019, **4**, 819–824.
49 B. J. Bohn, *et al.*, Boosting Tunable Blue Luminescence of Halide Perovskite Nanoplatelets through Postsynthetic Surface Trap Repair, *Nano Lett.*, 2018, **18**, 5231–5238.
50 D. P. Nenon, *et al.*, Design Principles for Trap-Free CsPbX 3 Nanocrystals: Enumerating and Eliminating Surface Halide Vacancies with Softer Lewis Bases, *J. Am. Chem. Soc.*, 2018, **140**, 17760–17772.
51 V. G. V. Dutt, S. Akhil, R. Singh, M. Palabathuni and N. Mishra, Year-Long Stability and Near-Unity Photoluminescence Quantum Yield of $CsPbBr_3$ Perovskite Nanocrystals by Benzoic Acid Post-treatment, *J. Phys. Chem. C*, 2022, **126**, 9502–9508.
52 C. Liu, *et al.*, Transparent Ultra-High-Loading Quantum Dot/Polymer Nanocomposite Monolith for Gamma Scintillation, *ACS Nano*, 2017, **11**, 6422–6430.